*International Journal of Thermophysics, Vol. 18, No. 1, 1997*

# Measurements of the Thermal Diffusivity of Aluminum Using Frequency-Scanned, Transient, and Rate Window Photothermal Radiometry. Theory and Experiment

**E. MacCormack,[1] A. Mandelis,[1,2] M. Munidasa,[1] B. Farahbakhsh,[3] and H. Sang[3]**

*Received February 8, 1996*

The thermal diffusivity of various types of aluminum has been measured, using a completely noncontact experimental configuration based on infrared photothermal radiometry. Photothermal response transients, conventional frequency scans, and pulse duration- or repetition rate-scanned rate windows have been investigated. It has been shown that the conventional frequency scan is not suitable for measurements of aluminum with a short thermal transport time such as foils, due to an extremely degraded signal-to-noise ratio (SNR). Also, it has been found that the conventional frequency scan method is less sensitive to the actual value of thermal diffusivity than the rate-window scan. The rate-window method, furthermore, gives superior SNR especially for thin metals and yields excellent agreement between the theory and the data. An advantage of the pulse duration-scanned rate window mode is that it does not require knowledge of the instrumental transfer function as an input. The transient response gives the worst SNR but is best for the physical interpretation of the photothermal signals. In addition, it has been shown that the infrared photothermal radiometric transmission mode is less sensitive to surface roughness than the reflection mode and, therefore, is preferable for thermal diffusivity measurements of aluminum and of good thermal conductors, in general.

**KEY WORDS:** aluminum; heat transfer coefficient; photothermal radiometry; thermal diffusivity.

[1] Photothermal and Optoelectronic Diagnostics Laboratory and Manufacturing Research Corporation of Ontario (MRCO), Department of Mechanical Engineering, University of Toronto, Toronto, Ontario M5S 1A4, Canada.

[2] To whom correspondence should be addressed.

[3] Alcan International Ltd. Research Laboratories, Kingston, Ontario K7L 5L9, Canada.



0195-928X/97/0100-0221$12.50/0 

## 1. INTRODUCTION

There has been a renewed interest in developing new methods of determining the thermal diffusivity of materials in recent years. For metals, in particular, this is largely a result of many new applications at elevated temperatures.

Thermal diffusivity is a thermophysical property which gives both direct and indirect information on materials. The direct knowledge of the thermal diffusivity of a material facilitates the modeling of the cooling and heating of machinery, heat-resistant coatings, heat sinks, or spreaders. Also, indirect information (i.e., specific heat, effusivity or the thickness of the coating in some cases) provided by thermal analysis is very useful for the nondestructive depth profiling of surface-modified metals [1] and, potentially, for the quality control of manufactured metal sheets. Apart from its own importance, determination of the thermal diffusivity of a material, $\alpha$, also yields the value of the thermal conductivity, $k$, of a material, with known density $\rho$ and specific heat $c$, from [2, 3]

$$\alpha = k/\rho c \tag{1}$$

Thermal diffusivity is determined by dynamic (time-dependent) heat flow methods. These methods are characterized by their relative speed and accuracy and have increasingly become more popular than the steady-state conductivity measurements.

Three signal generation and detection photothermal techniques have been used and compared in this work to determine experimentally the thermal diffusivity of aluminum: conventional periodic, transient, and novel hybrid heat-flow methods. In the periodic thermal-wave method, a sample of known thickness is irradiated with a harmonically modulated laser beam, and the periodic temperature at the front or at the back surface of the sample is monitored at several modulation frequencies (frequency-scan method). The frequency-dependent thermal diffusion length is $\mu(f) = (\alpha/\pi f)^{1/2}$ (Ref. 3, Chap. 2.6), where $f$ is the modulation frequency. $\mu(f)$ is related to the phase lag of the detected temperature (thermal) wave with respect to the heat source, which may be monitored using a lock-in amplifier. Thermal diffusivity can be calculated directly from the phase of the photothermal signal. In the transient photothermal heat flow method,[4] a sample of known thickness is irradiated on one side with a laser pulse; then the evolution of the temperature on either side is monitored and the rate of decay is related to the diffusivity.

Photothermal rate-window (RW) spectrometry [5] is a new technique which combines the simplicity of the interpretation of time-domain measurements and the high-precision measurement feature of the rate-window

extremum. When using a lock-in amplifier (LIA) to set up the rate window, the technique exhibits a superior signal-to-noise ratio (SNR) even when used with infrared photothermal radiometry at low temperatures [6]. The output signal $e_{\text{out}}(T_0)$ of a linear filter responding to a transient input signal $e_{\text{in}}(t)$ can be determined by a periodic reference signal $e_{\text{rw}}(t, T_0)$, which establishes the rate window over the pulse repetition period $T_0$

$$e_{\text{out}}(T_0) = 1/T_0 \int_0^{T_0} e_{\text{in}}(t)\, e_{\text{rw}}(t, T_0)\, dt \tag{2}$$

Photothermal RW detection with a LIA as a filter and demodulator yields the fundamental coefficient of the Fourier series into which the repetitive input transient thermal waveform may be expanded [7]. As such it can be labeled as a technique intermediate between frequency and time domains ("hybrid"). The RW technique is a derivative operation method for measuring the decay time constant of the thermal transient. By matching the instrumentally set RW to the decay time constant of the transient through scanning the period or pulse duration, one measures the thermal diffusivity of the sample from the maximum of the resulting RW signal. The maximum position of the RW signal is very sensitive to the thermophysical properties of the sample because of the derivative nature of the method.

A popular photothermal technique well suited for noncontact thermal analysis of solids is photothermal radiometry (PTR) [8, 9]. It relies on the detection of variations in the infrared thermal radiation emitted from a sample that is excited by electromagnetic radiation (typically from a laser) of modulated intensity. The temperature of the sample increases as the result of the optical energy absorption and subsequent nonradiative de excitation. A simple theory of PTR was given by Nordal and Kanstad [8], who introduced the technique. The radiant energy $W$ per unit area emitted from a gray body of emissivity $\varepsilon$ and absolute temperature $T$ is given by the Stefan–Boltzmann law:

$$W = \varepsilon \sigma T^4 \tag{3}$$

where $\sigma$ is the Stefan–Boltzmann constant $\varepsilon = 1$ corresponds to an ideal blackbody. If an opaque solid is irradiated by an optical pulse of energy $E$ at wavelength $\lambda$ that is absorbed at the surface of the body, resulting in a small temperature rise $\delta T(E)$, the total radiant energy is increased by

$$\delta W(E) \approx 4\varepsilon \sigma T_\infty^3\, \delta T(E) \tag{4}$$

provided that $\delta T \ll T_\infty$ ($T_\infty$ is the background solid temperature from which the excursion $\delta T$ occurs).

Back-scattered PTR is sensitive mostly to the sample surface temperature rather than to the bulk temperature, provided that the sample is opaque in the wavelength range used for detection. It is therefore used to measure directly the sample surface temperature without regard to the size or thickness or shape. Transmission PTR is sensitive to both the surface and the bulk of the sample in which conduction heat transfer occurs.

The purpose of this work is to compare frequency-scanned, transient, and RW photothermal radiometric techniques regarding their ability to measure the thermal diffusivity of various types of aluminum, as representatives of a class of difficult-to-measure, high-thermal conductors. A reliable model for interpretation of the data has also been developed.

Two variations of the PTR lock-in RW spectrometry have been used: a pulse duration scan and a period scan. In the pulse duration-scan method, the period of the modulation is constant (a single frequency), while the pulse duration is scanned. Therefore, the inherent advantage of pulse duration-scanned RW spectrometry lies in the invariance of the instrumental transfer function during the experiment [7].

## 2. INSTRUMENTATION AND METHODOLOGY

A schematic diagram of the experimental system used for all photothermal radiometric measurements in both modes (reflection and transmission) is shown in Fig. 1. An $Ar^+$ laser (INNOVA-100-15) operating at 514.5 nm and with a purely $TEM_{(0)}$ mode having modulated power up to 300 mW on the sample surface was employed as the thermal waveform generator. The spatial resolution of the experiments was limited by the spot-size of the laser beam.

The laser was modulated by an acoustooptic (A/O) modulator (ISOMET 1201E-1). The beam spot size on the sample surface was 10 mm, unless otherwise stated. This allowed the comparison of the photothermal data with a one-dimensional heat diffusion model. Removable mirrors were used to direct the beam on either the front or the back surface of the sample. The blackbody radiation emitted by the sample surface was collected and focused onto the detector using off-axis paraboloidal mirrors. The heated area of the sample surface was centered around the focal plane of one mirror and the detector was at the focal point of the other mirror, Fig. 1.

The detector was a liquid nitrogen-cooled photoconductive HgCdTe [mercury–cadmium–telluride (MCT) sensor; EG&G Judson Model J15D16-M204] with an active area of 1 $mm^2$ and a spectrally sensitive range of 2–24 $\mu$m. A germanium window with a transmission bandwidth of 2–13 $\mu$m was mounted in front of the detector to block any visible radiation from the pump laser.

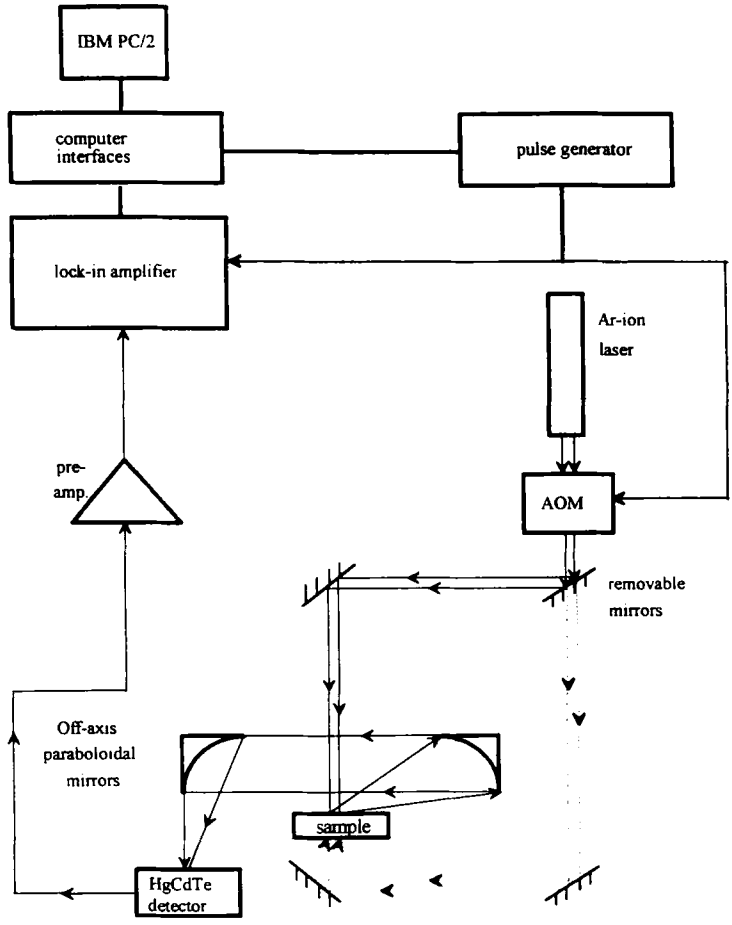


Fig. 1. Schematic diagram of the experimental setup for both backscattering (laser beam represented by solid lines) and transmission (laser beam represented by dashed lines) photothermal radiometry measurements.

The signal was amplified by a compatible preamplifier (EG&G Judson Model PA-350) before being fed to the digital LIA (Stanford Research System Model SR850). A "coarse adjustment" resistor was installed in the preamplifier to compensate roughly for the dc offset level produced by the detector in the absence of the radiometric signal. Since this dc offset changes with time and background conditions, periodic manual tuning was allowed for.

For measurements of transient signals, a fixed period was used with a specified pulse duration. Coadded and averaged data were collected using

an HP 54200D digitizing oscilloscope instead of the LIA. By using different software programs to generate pulses for the A/O modulator to control the pulse profile, duration, frequency, or repetition period, frequency scans, square pulses, or RW scans could be easily implemented.

## 3. MATERIALS

Steel and a zirconium–niobium alloy used in the nuclear pressure tube industry were used primarily to test the theoretical formalism and as a reference for an instrumental phase correction or for comparison with aluminum samples.

The dimensions of the Zr–Nb sample were $25.4 \times 25.4 \times 4$ mm$^3$. It was considered a semiinfinite metal in these measurements. Steel samples (stainless steel 304) used in the present work included a "semiinfinite" sample $50 \times 50 \times 50$ mm$^3$ and three samples of "finite" thicknesses of 0.25, 0.5, and 0.75 mm, respectively.

Three kinds of aluminum samples were also used. The first was the well-known commercial AA6061-T6 aluminum alloy, designated here "Group 1." Five square samples, $25.4 \times 25.4$ mm$^2$, of different thicknesses were machined from a homogeneous piece.

Another kind of sample was aluminum foils and thin layers [10], designated "Group 2." This group included several alloy samples of varying thicknesses: type AA1145-H18 (hard rolled) and type AA1 100-O (soft rolled). The concentration of pure aluminum in the former was at least 99.45%; in the latter it was 99.0%.

The third group, "Group 3," consisted of a plate of single crystal aluminum [10]. The plate comprised five regions having different grain normal orientations and a mean thickness of 2.5 mm. The orientations of

**Table I.** Group 3 Orientations of Grain Normals w.r.t. Horizontal Axes of Single-Crystal Aluminum[a]

| Region No. | Thickness (mm) | $\Theta$ (deg) | $\Phi$ (deg) | Thermal diffusivity ($10^{-5}$ m$^2 \cdot$ s$^{-1}$) |
|---|---|---|---|---|
| 1 | 2.5 | 41.1 | 47.5 | $8.3 \pm 0.1$ |
| 2 | 2.53 | 17.8 | 16.6 | $9.4 \pm 0.1$ |
| 3 | 2.51 | 10.1 | 22.3 | $9.5 \pm 0.1$ |
| 4 | 2.51 | 4.1 | 9.8 | $9.5 \pm 0.1$ |
| 5 | 2.55 | 5.4 | 1 | $9.5 \pm 0.1$ |

[a] For the definitions of $\Theta$ and $\Phi$, see Fig. 2. The thermal diffusivity values were obtained using pulse duration-scanned rate-window transmission PTR.

the normals were determined by the back-scattered X-ray Laue method and are shown in Table I. It can be seen from the stereographic projection in Fig. 2 that grain 1 lies almost parallel to the $\langle 111 \rangle$ crystallographic direction, whereas most of the other grains are closer to the $\{100\}$ plane. The crystal structure of aluminum is face-centered cubic (FCC) with a coordination number of 12, the most efficient packing factor of which is 0.74. The most close-packed direction in FCC is the $\langle 100 \rangle$ and the most close-packed plane is the $\{111\}$.

Since the thermophysical properties depend on both the structure and the processing history of metals, in order to obtain good radiometric SNR

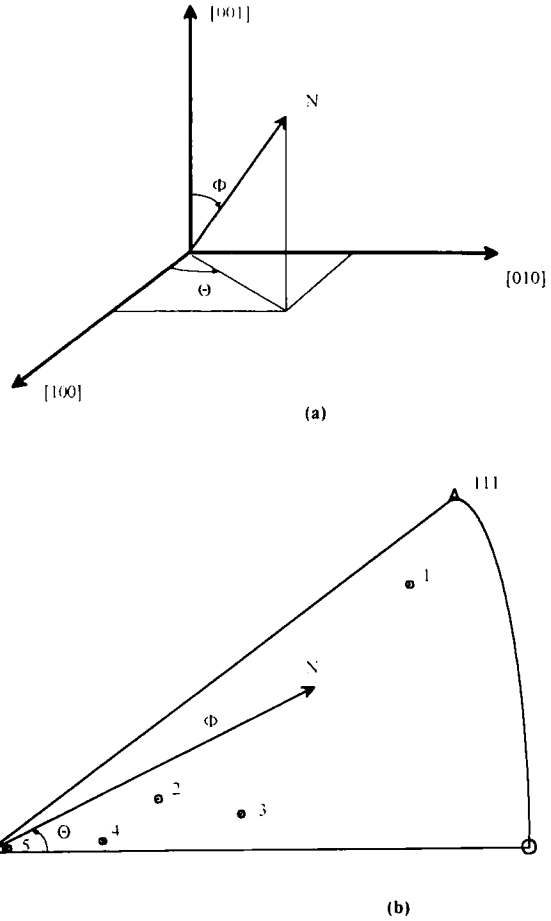


Fig. 2. (a) Crystallographic coordinates: and (b) Stereographic projection of an Al plate with five single-crystal grains.

and reliable data, both surfaces of all samples were kept smooth and clean. Experiments with some aluminum samples indicated that controllability of the surface condition was extremely important for thermal diffusivity measurements. The backscattering detection mode proved to be especially sensitive to this factor. Therefore thorough cleaning with methanol and polishing with fine-grain sandpaper of these surfaces were required before the experiments. On the other hand, good agreement between theoretical predictions and experimental data from metals with a lower thermal diffusivity, steel and Zr–Nb, was achieved without polishing, but only cleaning, in order to get better signals and reproducible data.

## 4. THEORETICAL

### 4.1. Time-Domain Heat Conduction Boundary Value Problem

#### *4.1.1. Single Pulse Response*

According to Eq. (4), the PTR signal is expected to be proportional to the surface temperature excursion $\delta T \equiv \Theta(\mathbf{r}=0, t) = T(\mathbf{r}=0, t) - T_s$ for small thermal perturbations in a solid.

Existing theoretical models failed to predict the experimental responses of the aluminum samples to the photothermal source. Therefore, it became necessary to construct an appropriate one-dimensional heat diffusion model to calculate the thermal diffusivity of aluminum, which would also be capable of describing the responses of steel and Zr–Nb alloy as special cases. The major problem with the existing models appeared to be the assumption of adiabatic boundary condition at the solid–gas interface [4]:

$$\frac{\partial}{\partial x}\Theta(x, t)\big|_{x=0} = 0 \tag{5}$$

However, discrepancies between the adiabatic theory and the experimental data clearly indicated the presence of some interfacial heat loss and the need to change boundary conditions by taking a phenomenological "radiation" boundary condition into consideration [3]. The one-dimensional diffusion equation governing the evolution of the position ($x$) and time ($t$)-dependent translated temperature $\Theta(x, t)$ inside the sample in Fig. 3 after the absorption and nonradiative energy conversion of the light is

$$\frac{\partial^2\Theta(x, t)}{\partial x^2} - \frac{1}{\alpha}\frac{\partial\Theta(x, t)}{\partial t} = 0 \tag{6}$$

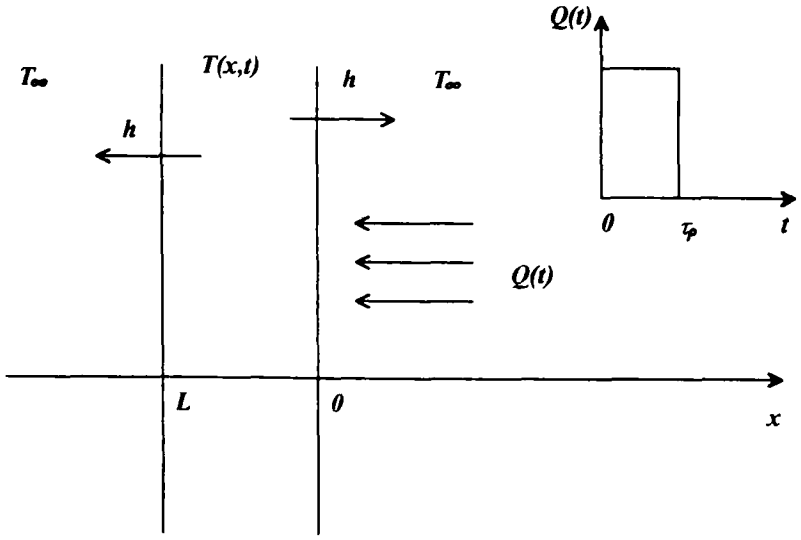


Fig. 3. One-dimensional geometry for the heat conduction problem in a solid with thermal diffusivity $\alpha$, thermal conductivity $k$, heat transfer coefficient $h$, and thickness $L$. $Q(t)$ represents the heat flux at the solid-gas interface $x=0$. The inset shows the temporal lineshape of $Q(t)$ for pulsed PTR.

with the following boundary conditions

$$-k\frac{\partial\Theta(x,t)}{\partial x} = -h\Theta(0,t) + Q(t), \qquad x=0 \tag{7a}$$

$$-k\frac{\partial\Theta(x,t)}{\partial x} = h\Theta(L,t), \qquad x=L \tag{7b}$$

where $h$ is a phenomenological (most likely composite) "radiation" heat transfer coefficient.

Theoretical consideration of the convective part of the heat transfer coefficient can be performed through calculation of the Grashof number. The Grashof number (Gr) represents the ratio of buoyant to viscous forces and controls the rate of heat transfer for free convection [11]:

$$\mathrm{Gr} = \beta^* g(T_s - T_\infty)\, d^3/\nu^2 \tag{8}$$

where $\beta^*$ in $\mathrm{K}^{-1}$ is the coefficient of thermal expansion, $g$ is the acceleration of gravity (9.81 $\mathrm{m\cdot s^{-2}}$), $d$ is the diameter of the solid–gas interface in cm, and $\nu$ is the kinematic viscosity of air ($1.568\times10^{-5}$ $\mathrm{m^2\cdot s^{-1}}$). Under

maximal surface heating through a square pulse of duration $t$, the rise in the surface temperature can be written

$$\delta T(t) = \frac{Q^* \sqrt{t}}{\sqrt{\rho c k}} \tag{9}$$

where $Q^*$ is the modulated laser power ($3000\ \mathrm{W \cdot m^{-2}}$), and $\rho$, $c$, and $k$ are thermophysical properties of the sample (for Al, $\rho = 2700\ \mathrm{kg \cdot m^{-3}}$, $c = 1006\ \mathrm{J \cdot kg^{-1} \cdot K^{-1}}$, and $k = 200\ \mathrm{W \cdot m^{-1} \cdot K^{-1}}$) [12]. Since the temperature ($T = 300$ K) does not change significantly in the experiments ($\delta T$ is 0.13 K), the heated spot diameter is small, and the coefficient of a thermal expansion (for air) is proportional to $1/T$, it is found that $\mathrm{Gr} \approx 17$. For a Grashof number less than 2000 the convective part of the heat transfer coefficient is practically nonexistent [11], therefore convection may be ignored. A recent PTR study of solid–gas interfacial convection has measured convective $h$ values consistent with the foregoing calculation of the Grashof number [13]. Further discussion of the physical nature of the phenomenological $h$ coefficient is presented later.

There are several analytical methods for solving the boundary value problem of Eqs. (6) and (7). Green's function method is a convenient one. For a thermal field with a bulk source $\rho(x, t)$, one obtains [14]

$$\begin{aligned}\Theta(x, t) = {} & \frac{\alpha}{k} \int_0^{t^+} dt_0 \int_{x_0} G(x, t \mid x_0, t_0)\, \rho(x_0, t_0)\, dx_0 \\ & + \alpha \int_0^{t^+} dt_0 \iint_S \left[ G(x, t \mid x_0, t_0) \frac{\partial}{\partial n_0} \Theta(x_0, t_0) - \Theta(x_0, t_0) \right. \\ & \left. \times \frac{\partial}{\partial n_0} G(x, t \mid x_0, t_0) \right] dS \\ & + \int_x \Theta(x_0, 0)\, G(x, t \mid x_0, 0)\, dx_0 \end{aligned} \tag{10}$$

where $n_0$ is the inward normal to the spatial region defined by the solid volume. $S$ is the surface surrounding this volume. In the 1-D geometry in Fig. 3, $S$ degenerates to the two points $x = 0$, $L$. Therefore, in the absence of the bulk sources, $\rho(x, t) = 0$, and Eq. (10) becomes

$$\Theta(x, t) = \int_0^L \Theta(x_0, 0)\, G(x, t \mid x_0, 0)\, dx_0 + \frac{\alpha}{k} \int_0^{t^+} G(x, t \mid 0, t_0)\, Q(t_0)\, dt_0 \tag{11}$$

When expanded in terms of eigenfunctions of the boundary value problem of Eqs. (6) and (7), Green's function can be written [15]

$$G(x, t \mid x_0, t_0) = \sum_n e^{-\alpha\lambda_n^2(t-t_0)} u_n(x)\, u_n(x_0) \tag{12}$$

In order to obtain the eigenfunction set $\{u_n\}$ and the corresponding eigenvalue spectrum $\{\lambda_n\}$ the following auxiliary equation was taken into consideration:

$$\frac{d^2u_n(x)}{dx^2} + \lambda_n^2 u_n(x) = 0 \tag{13}$$

subject to the boundary conditions

$$k \left.\frac{du_n(x)}{dx}\right|_{x=0} = hu_n(0) \tag{14a}$$

and

$$-k \left.\frac{du_n(x)}{dx}\right|_{x=L} = hu_n(L) \tag{14b}$$

The solution to this auxiliary boundary value problem leads to the following eigenvalue equation:

$$2\cot(\lambda_n L) = \frac{\lambda_n L}{Bi} - \frac{Bi}{\lambda_n L} \tag{15}$$

where Bi is the Biot number defined as

$$Bi \equiv \frac{hL}{k} \tag{16}$$

Equation (15) was solved numerically as a system of two equivalent equations calculated simultaneously using the bisection method [16]:

$$\tan\left(\frac{\lambda_n L}{2}\right) = \frac{Bi}{\lambda_n L} \tag{17a}$$

and

$$\cot\left(\frac{\lambda_n L}{2}\right) = -\frac{Bi}{\lambda_n L} \tag{17b}$$

The eigenvalues in the representation of Eqs. (17a) and (17b) were tabulated by Carslaw and Jaeger [3]. The eigenvalues obtained with the bisection method fully agree with those values. Though either Eq. (15) or Eqs. (17a) and (17b) can be used in calculations, using the system of two equations [16] proved to be numerically simpler, with the added advantage that the calculated values can be readily checked against the reference [3]. Although there is no limitation on the number of roots of the transcendental equations (15) and (17), in this work the number of calculated eigenvalues for each Biot number was restricted to 10. The reason for this limitation was purely numerical; however, it was verified that this number was sufficient for the photothermal signal to saturate.

The eigenfunction set $\{u_n\}$ is given by

$$u_n(x) = \cos(\lambda_n x) + M_n \sin(\lambda_n x) \tag{18}$$

where

$$M_n = \frac{Bi}{\lambda_n L} \tag{19}$$

$\{u_n\}$ can be shown to be orthogonal for $x \in [0, L]$ and therefore forms a basis for the expansion of any function of $x$. To make it orthonormal, the condition

$$K_n^2 \int_0^L u_n^2(x)\, dx = 1 \tag{20}$$

may be defined, leading to orthonormal eigenfunctions,

$$u_n(x) = K_n[\cos(\lambda_n x) + M_n \sin(\lambda_n x)] \tag{21}$$

where

$$K_n = \frac{1}{\sqrt{\int_0^L u_n^2(x)\, dx}} \tag{22}$$

Performing the integration in Eq. (22) and substituting Eq. (21) into Eq. (12) yields

$$G(x, t \mid x_0, t_0) =$$

$$2 \sum_{n=1}^{\infty} \left\{ \frac{[\cos(\lambda_n x) + M_n \sin(\lambda_n x)] \cdot [\cos(\lambda_n x_0) + M_n \sin(\lambda_n x_0)]}{(1 + M_n^2) L + 1/(2\lambda_n)\{(1 - M_n^2) \sin(2\lambda_n L) + 2M_n[1 - \cos(2\lambda_n L)]\}} \right\}$$

$$\times e^{-\alpha \lambda_n^2 (t - t_0)} \tag{23}$$

Assuming the initial condition $\Theta(x, 0)=0$ and using Eq. (23) in Eq. (11) gives the following expression for the photothermal field:

$$\Theta(x, t)=\frac{\alpha}{k}\int_0^t G(x, t\,|\,0, t_0)\, Q(t_0)\, dt_0 =$$

$$\frac{2\alpha}{k}\sum_{n=1}^{\infty}\left[\frac{\cos(\lambda_n x)+M_n\sin(\lambda_n x)}{(1+M_n^2)\,L+1/(2\lambda_n)\{(1-M_n^2)\sin(2\lambda_n L)+2M_n[1-\cos(2\lambda_n L)]\}}\right]$$

$$\times e^{-\alpha\lambda_n^2 t}\int_0^t Q(t_0)\, e^{\alpha\lambda_n^2 t_0}\, dt_0 \tag{24}$$

*4.1.2. Infinite Pulse-Train Response*

Further calculations were performed taking into account the experimental fact that one deals with a superposition of an infinite number of prior pulses forming the dynamic steady-state background value of transient photothermal signals. Defining

$$J(t)\equiv\int_0^t Q(t_0)\, e^{\alpha\lambda_n^2 t_0}\, dt_0 \tag{25}$$

then extending the time interval $[0, t]$ to include all $(m)$ earlier transients, of duration $\tau_p$ and repetition period $T_0$, $J(t)$ becomes

$$j(t)=Q_0\left\{\int_0^{\tau_p} e^{\alpha\lambda_n^2 t_0}\, dt_0+\int_{T_0}^{T_0+\tau_p} e^{\alpha\lambda_n^2 t_0}\, dt_0\right.$$

$$\left.+\cdots+\int_{mT_0}^{mT_0+\tau_p} e^{\alpha\lambda_n^2 t_0}\, dt_0\right\} \tag{26}$$

At the end of $(m-1)$ prior pulses, when $m\geqslant 1$, $J(t)$ can be shown to be

$$J_m[t=(m-1)\,T_0]=\frac{Q_0(e^{\alpha\lambda_n^2\tau_p}-1)}{\alpha\lambda_n^2}\sum_{j=0}^{m-1} e^{\alpha\lambda_n^2 jT_0} \tag{27}$$

Hence,

$$e^{-\alpha\lambda_n^2 t}J_m(t)|_{t=(m-1)T_0}=\frac{Q_0}{\alpha\lambda_n^2}\left[\frac{1-e^{-(m-1)\alpha\lambda_n^2 T_0}}{1-e^{-\alpha\lambda_n^2 T_0}}\right](e^{\alpha\lambda_n^2\tau_p}-1) \tag{28}$$

The limit of Eq. (28) when $m\to\infty$ is

$$\lim_{m\to\infty}\{e^{-\alpha\lambda_n^2(m-1)T_0}J_m[(m-1)\,T_0]\}=\frac{Q_0}{\alpha\lambda_n^2}\left(\frac{e^{\alpha\lambda_n^2\tau_p}-1}{1-e^{-\alpha\lambda_n^2 T_0}}\right) \tag{29}$$

and therefore at time $\Delta t$ after an infinite pulse train, the factor $e^{\alpha\lambda_n^2 t}J(t)$ in Eq. (24) can be written compactly as

$$e^{\alpha\lambda_n^2 t}J(t) = \frac{Q_0}{\alpha\lambda_n^2}\left(\frac{e^{\alpha\lambda_n^2\tau_p}-1}{1-e^{\alpha\lambda_n^2 T_0}}\right)e^{-\alpha\lambda_n^2 t}\int_0^{t_0} Q(t_0)\,e^{\alpha\lambda_n^2 t_0}\,dt_0 \tag{30}$$

The final expression for $\Theta(x, \Delta t)$, for times shorter or longer than the pulse duration, is

$$\Theta(x,\Delta t) = \frac{2Q_0}{k}\sum_{n=1}^{\infty}\frac{1}{\lambda_n^2} \times\left[\frac{\cos(\lambda_n x)+M_n\sin(\lambda_n x)}{(1+M_n)^2 L+(1/2\lambda_n)\{(1-M_n^2)\sin(2\lambda_n L)+2M_n[1-\cos(2\lambda_n L)]\}}\right] \times\begin{cases}\left(\dfrac{e^{\alpha\lambda_n^2\tau_p}-1}{e^{\alpha\lambda_n^2 T_0}-1}\right)e^{-\alpha\lambda_n^2\Delta t}+1-e^{-\alpha\lambda_n^2\Delta t}, & \Delta t\leqslant\tau_p\\ \left(\dfrac{e^{\alpha\lambda_n^2\tau_p}-1}{e^{\alpha\lambda_n^2 T_0}-1}\right)e^{\alpha\lambda_n^2 T_0}e^{-\alpha\lambda_n^2\Delta t}, & \Delta t\geqslant\tau_p\end{cases} \tag{31}$$

The infinite pulse train (number of prior pulses) included in Eq. (31) can be readily used in the analysis of photothermal transients obtained from either back scattered ($x=0$) or transmission ($x=L$) PTR.

### 4.2. Frequency-Domain Heat Conduction Boundary Value Problem

The 1-D diffusion boundary value problem defined by Eqs. (6) and (7) can be solved in the frequency domain using a combined Laplace–Fourier method. Defining the Laplace transform of the temperature field in the usual manner,

$$\hat{\Theta}(x,s) = \int_0^{\infty} e^{-st}\Theta(x,t)\,dt \tag{32}$$

transforms the boundary value problem as follows:

$$\frac{d^2\hat{\Theta}(x,s)}{dx^2} - \sigma^2\hat{\Theta}(x,s) = 0, \qquad \sigma=\sqrt{s/\alpha} \tag{33}$$

with

$$-k\frac{d\hat{\Theta}(0,s)}{dx} = \hat{Q}(s) - h\hat{\Theta}(0,s) \tag{34a}$$

and

$$-k\frac{d\hat{\Theta}(L,s)}{dx}=h\hat{\Theta}(L,s) \tag{34b}$$

The solution for the system of Eqs. (33) and (34) when evaluated at $x=0$, $L$ is, respectively,

$$\hat{\Theta}(0,s)=\hat{Q}(s)\left[\frac{(k\sigma+h)+(k\sigma-h)\,e^{-2\sigma L}}{(k\sigma+h)^2-(k\sigma-h)^2\,eL}\right] \tag{35a}$$

and

$$\hat{\Theta}(L,s)=\frac{2k\sigma\hat{Q}(s)\,e^{-\sigma L}}{(h+k\sigma)^2-(k\sigma-h)^2\,e^{-2\sigma L}} \tag{35b}$$

Now a Fourier representation of Eqs. (35a) and (35b) may be obtained in the frequency domain by letting $s\to i\omega$, so that $\sigma=(i\omega/\alpha)^{1/2}$ and $\hat{Q}(s)\to Q(t)=(I_0/2)\,e^{i\omega t}$.

Using these expressions for $\sigma$ and $Q(t)$, Eqs. (35a) and (35b) can be written as

$$\Theta(0,t)=\frac{I_0}{2k(\sigma+h/k)}\left[\frac{1+\gamma e^{-2\sigma L}}{1-\gamma^2 e^{-2\sigma L}}\right]e^{i\omega t} \tag{36a}$$

and

$$\Theta(L,t)=\frac{\sigma I_0}{k(\sigma+h/k)}\left[\frac{e^{-\sigma L}}{1-\gamma^2 e^{-2\sigma L}}\right]e^{i\omega t} \tag{36b}$$

where

$$\begin{aligned}\gamma&=[\sigma-(h/k)]/[\sigma+(h/k)]\\&=\frac{1}{1+(\omega\tau_h)^2}\{(1-\omega\tau_h\sqrt{2\omega\tau_h}-[1-(\omega\tau_h)^2]\\&\quad+i[-2\omega\tau_h+(1+\omega\tau_h)\sqrt{2\omega\tau_h}]\}\equiv I+iQ\end{aligned} \tag{37}$$

In order to simplify the numerical calculations and facilitate the theoretical fits to the data in the form of PTR signal amplitude and phase polar coordinate representations of Eq. (37) were obtained.

## 5. EXPERIMENTAL PROCEDURE AND RESULTS

### 5.1. PTR Signal Generation and Characterization

To study the dependence of the experimental results on the laser beam size and thus assess the dimensionality of the problem, experiments were performed with semiinfinite AA6061-T6 aluminum from Group 1 and with the semiinfinite Zr–Nb alloy. Both samples were irradiated by laser beams of different sizes and data were obtained in the reflection mode of the frequency scan. The frequency range was from 10 to 210 Hz. Figure 4 shows the dependence of the modulated signal on the laser beam size. The PTR phase was used as the criterion for attaining 1-D behavior, rather than the PTR amplitude, because the former is more sensitive to dimensionality [17], becoming independent of modulation frequency in the 1-D limit for a semi infinite solid. [18]. It can be noted that for the Zr–2.5Nb alloy the phase of the signal remains flat for both 5- and 10-mm spot sizes and, therefore, can be treated with the 1-D theory of Section 4, even at the lowest frequencies. On the other hand, the aluminum sample demonstrates essentially no difference under excitation with spot sizes 10 and 15 mm, and 3-D effects are evident [19] for $f < 20$ Hz. For the smaller, 5-mm, spot-size beam, very prominent 3-D effects occur in the frequency range $< 90$ Hz. Figure 4 establishes that, in order to maintain the one dimensionality of

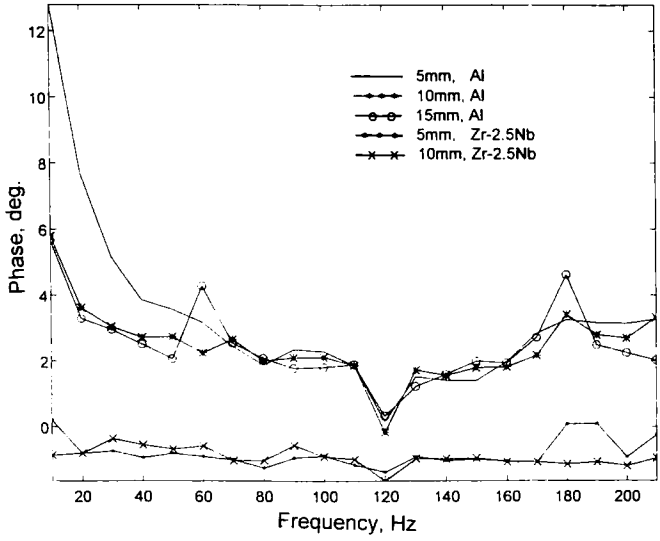


**Fig. 4.** The frequency scan dependence of semiinfinite aluminum and reference metals on the laser-beam size.

the problem with aluminum, the laser beam size should be at least 10 mm, provided the frequency range is higher than 20–30 Hz. In the time domain, this corresponds to detection times $t \leqslant 20$ ms.

Special care was taken to show that there was no convection or, strictly speaking, that the convective part of the heat transfer coefficient was negligible and should not be taken into consideration in calculations, as predicted from Eq. (8). Experiments were performed with and without a cooling fan, using samples of various members of Groups 1–3 under identical conditions. The results demonstrated that only the magnitude of the signal decreased with the cooling fan, and *not* the PTR transient shape or the PTR frequency response. This is consistent with the simple lowering of the background (dc) temperature of the metal samples without change of the dynamic evolution of their optically generated thermal contents, which implies no convective heat-loss enhancement at the cooled interface. Therefore, any effects of forced or natural convection during the PTR experiments were deemed negligible, in agreement with the calculation of the Grashof number, Eq. (8).

Finally, it is essential for the interpretation of PTR signals that the detected responses be linearly proportional to the surface temperature, due to the strong nonlinearity of Eq. (3). The output voltage of an IR detector which detects a narrow spectral bandwidth, such as in the present situation may be written as [1, 20]

$$V = CT^n \tag{38}$$

where $C$ is a constant that involves detector parameters, detection electronics, and the surface emissivity of the sample, as well as the angle of observation for smooth metallic surfaces. $T$ is the temperature in degrees Kelvin. The exponent $n$ in Eq. (42) is approximated by [21]

$$\begin{aligned} n &\approx 5\frac{\lambda_m}{\lambda_d} \qquad \text{for} \quad \frac{\lambda_d}{\lambda_m} \leqslant 2.5 \\ n-1 &\approx 2.5\frac{\lambda_m}{\lambda_d} \qquad \text{for} \quad \frac{\lambda_d}{\lambda_m} \geqslant 2.5 \end{aligned} \tag{39}$$

where $\lambda_m$ is the peak emission wavelength related to the operating temperature by Wien's law and $\lambda_d$ is the center wavelength of the detection bandwidth. If the temperature elevation $T$ is much smaller than the ambient temperature $T_x$, the signal increase over the initial level $V_0$ can be written as

$$V - V_0 = nCT_x^{n-1}T = AT \tag{40}$$

showing that the detected signal is linearly proportional to the surface temperature, in agreement with Eq. (4). An experiment was conducted with a semiinfinite aluminum sample to test the linear dependence of the laser intensity vs. the lock-in signal amplitude for various periods. The results are shown in Fig. 5. For the specified period the laser power was changed from 100 to 400 mW, and the corresponding photothermal LLA signal was recorded. Measurements were repeated for three periods, 20, 200, and 1000 ms, and it was shown that the dependence of the LLA PTR signal on laser intensity was linear throughout.

## 5.2. The Nature of the Heat Transfer Coefficient

For thin layers of low-diffusivity metals such as steel and Zr–Nb alloys, the LL4 RW pulse duration scan proved to be the most sensitive technique for thermal diffusivity measurements [18]. However, experiments with aluminum and copper have shown that there are some difficulties in measuring radiometrically the thermal diffusivity of high thermal conductors. It has been found that the effect of the surface roughness influences measurements and the value of the effective heat transfer coefficient, $h$. By improving surface conditions of the semiinfinite aluminum samples through polishing, its experimental lock-in rate window pulse duration curve approached that obtained from the semiinfinite Zr–Nb

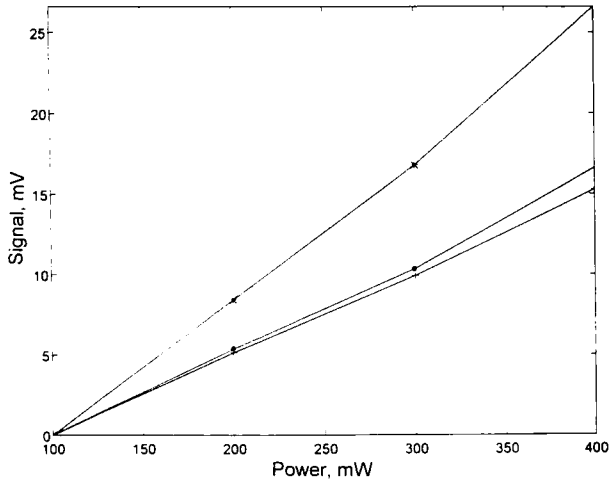


**Fig. 5.** Linear dependence of the laser power intensity versus the square wave-modulated lock-in signal amplitude for various periods. (+) $T_0 = 20$ ms; (●) $T_0 = 200$ ms; (★) $T_0 = 1000$ ms.

sample. Therefore, polishing of the sample surface decreases the value of the heat transfer $h$ coefficient, since the PTR data from the semiinfinite Zr–Nb sample obeyed the adiabatic boundary condition, which can be met in the model of Section 4 by setting $h \to 0$. Experimental curves of semi-infinite aluminum and Zr–Nb samples are shown in Fig. 6. The exact physical meaning of the effective heat transfer coefficient, $h$, however, remains unknown. It can be obtained empirically and it is undoubtedly affected by the enhanced heat transfer to the gas phase through the higher effective area of rough metal surfaces. Therefore, it is likely to be associated partly with a phenomenological surface thermal contact resistance [22] due to microscopic roughness, and accounts partly for radiation heat transfer effects [3].

The overall trend was for values of $h$ for the Zr–Nb sample to be much smaller than those for the Al sample. This was found to be rather general, indicating that for low-diffusivity materials, such as zirconium, the $h$ coefficient decreases and approaches the value for adiabatic boundary conditions. Limitations in numerical calculations yielded $h_{\min} = 10^3 \text{ W} \cdot \text{m}^{-2} \cdot \text{K}^{-1}$. Calculated photothermal signals with $h < h_{\min}$ were identical to that with $h = 10^3 \text{ W} \cdot \text{m}^{-2} \cdot \text{K}^{-1}$ and were labeled "adiabatic." In the case of steel samples, the 1-D theory with adiabatic boundary conditions ($\sim t^{1/2}$) also exhibited the best fit, while the RW fits indicated $h < h_{\min}$ and thus did not require knowledge of the $h$ coefficient.

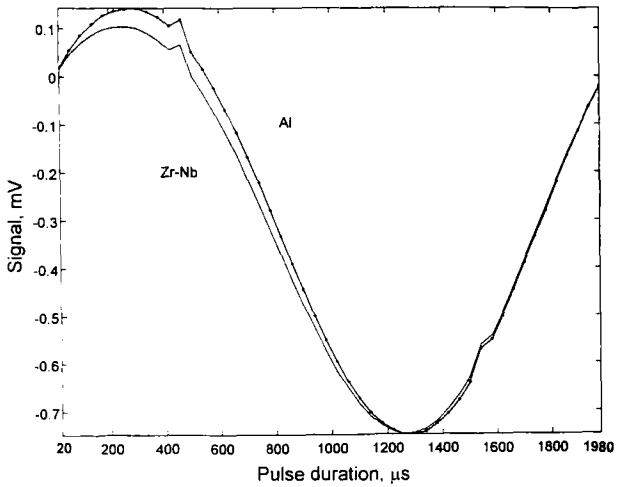


**Fig. 6.** The LIA RW quadrature pulse duration scan of semi infinite Al and Zr–Nb alloy samples for $T_0 = 2000\,\mu$s.

### 5.3. Thermal Diffusivity Measurements

The backscattered PTR transient signal from semiinfinite aluminum is very noisy, and it is practically impossible to extract meaningful values of thermal diffusivity from it. Furthermore, the values of $h$ obtained from backscattered PTR RW measurements exhibit great sensitivity to surface conditions and were found to be dependent on the repetition period $T_0$ of the experiment. Reliable $h$ values were determined using a polished semiinfinite aluminum sample and a theoretical fit of the data, to the limiting expression of Eq. (31) with $x=0$ and $L \to \infty$. In this limit it turns out [3] that the semiinfinite 1-D behavior is relatively insensitive to the actual value of $\alpha$, while it exhibits high sensitivity to $h$. In addition, the transient obtained from an aluminum sample of finite thickness in the PTR transmission mode can be a reliable source of the determination of $h$ values and for comparison with the results of the theoretical fit to the semiinfinite sample. In the case of the 2-mm-thick sample from Group 1 in the transmission mode for several values of $T_0$ and $\tau_p$, the value of $h$ obtained from the fit of the data to Eq. (31) was equal to $1 \times 10^5\ \mathrm{W \cdot m^{-2} \cdot K^{-1}}$. The reference value [23] of the thermal diffusivity of AA6061 aluminum alloy is $7 \times 10^{-5}\ \mathrm{m^2 \cdot s^{-1}}$. The foregoing $h$ value was essentially the same as that obtained from fitting the experimental transients from the Group 1, 1.2-mm-thick sample, to Eq. (31). Also the $h$ value for single crystal Al (Group 3, mean thickness $=2.5$ mm) in the transmission mode for $T_0 = 50$ ms and $\tau_p = 20$ ms was found to be the same as for all the above-mentioned samples ($\mathrm{h} = 1 \times 10^5\ \mathrm{W \cdot m^{-2} \cdot K^{-1}}$) for all single-crystal grain regions. These results show that in the PTR transmission mode the heat transfer coefficient $h$ does not depend sensitively on surface conditions, unlike the backscattered PTR data, fits to the theory, and it is not very sensitive to the actual value of $\alpha$.

Once the $h$ value was determined from the theoretical fits of Eq. (31) to the transient data using several pulse repetition period-duration ranges and a starting value of thermal diffusivity [2, 3], all aluminum samples were measured again using the lock-in rate window pulse duration scan, because of its superior SNR. Comparisons with frequency-scanned PTR were also made. Since the transmission mode was found to be less sensitive to surface roughness than the backscattered mode, it was used exclusively for thermal diffusivity measurements.

The extremum of the experimental curve is very sensitive to the value of thermal diffusivity, and by varying this value the best fit was found to the theory, Eq. (31), coupled to the $\tau_p$-scanned RW algorithm [7]. Both channels of the lock-in output (the in-phase and the quadrature) can be used in computations. However, the best fit and the most reliable values of

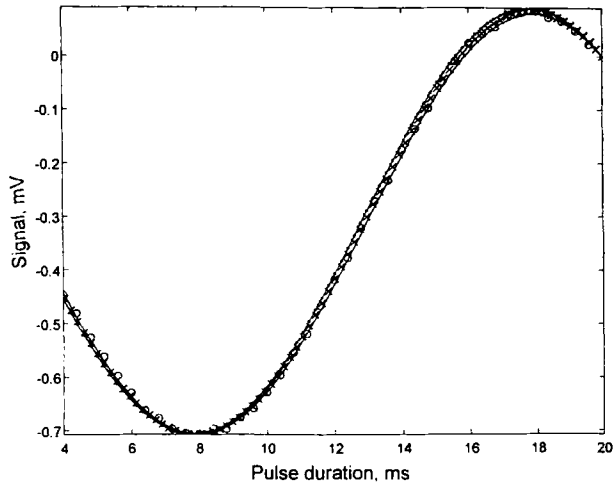


Fig. 7. The LIA RW pulse duration scan (quadrature) of AA6061-T6 Al alloy in the transmission mode; $L = 1.2$ mm; $T_0 = 20$ ms; $h = 1 \times 10^5$ W · m$^{-2}$ · K$^{-1}$. Circles, data; solid line, $\alpha = 7.7 \times 10^{-5}$ m$^2$ · s$^{-1}$; crosses, $\alpha = 7.5 \times 10^{-5}$ m$^2$ · s$^{-1}$; dotted line, $\alpha = 7.3 \times 10^{-5}$ m$^2$ · s$^{-1}$.

thermal diffusivity were obtained from the experimental channel, which exhibited two extrema. This depends on the period of modulation.

Figure 7 presents the LLN RW pulse duration scan of AA6061-T6 aluminum alloy (Group 1). Since the $h$ coefficient for all samples in Group 1 was found to be $1 \times 10^5$ W · m$^{-2}$ · K$^{-1}$, thermal diffusivity becomes the only fitting parameter. Furthermore, short pulse durations were more sensitive to thermal diffusivity. Therefore the first extremum of the experimental curve in Fig. 7 has been used in the fitting. Usually, the entire curve or at least the first half of it was fitted to the theory to extract the value of thermal diffusivity. Table II gives the value of the thermal diffusivity of AA6061-T6 aluminum alloy for three periods. As expected,

**Table II.** The Value of the Thermal Diffusivity of Group 1 AA6061-T6 Al Alloy Obtained from the Rate-Window $\tau_p$ Scan in the PTR Transmission Mode

| Period, $T_0$ (ms) | Thickness (mm) | Thermal diffusivity ($10^{-5}$ m$^2$ · s$^{-1}$) |
|---|---|---|
| 25 | 2 | $7.5 \pm 0.2$ |
| 20 | 1.2 | $7.5 \pm 0.2$ |
| 10 | 0.5 | $7.5 \pm 0.2$ |

the thermal diffusivity is the same for all samples from this group and it is consistent with the reference value of $7.0 \times 10^{-5} m^2 \cdot s^{-1}$ [23].

This measured value represents a "fine-tuning" of the reference value [23] originally assumed for the relevant transient to obtain the value of $h$. The constancy of $h$ across all samples and $(T_0, \tau_p)$ pairs with the same reference value of a in the transients, along with its relative insensitivity to the actual value of $\alpha$, implies that fine-tuning $\alpha$ with the high-SNR rate window technique will accurately yield at least meaningful *differences* in $\alpha$ among the various aluminum specimens with the same $h$ value. Figure 8 presents the LIA RW pulse duration scan of thin samples from Group 2 in the transmission mode. Since these samples are thin foils and the period employed is 1.5 ms, the SNR of experimental data is poorer than that for thick samples owing to the very low deposited thermal energy in the foils. Only the first half of the RW curve was fitted to the theory of Eq. (31) coupled to the $\tau_p$-scanned RW algorithm [7]. The $h$ value was taken to be $1 \times 10^5 W \cdot m^{-2} \cdot K^{-1}$, as calculated from transients in the transmission mode. The poor flit of the theory to the data in the vicinity of the second extremum in Fig. 8 is most likely due to surface roughness contributions to the PTR signal and bulk inhomogeneities of the thermophysical properties. Table III presents the resulting values of the thermal diffusivity of aluminum foils. The value of thermal diffusivity of the hard-rolled alloy was found to be significantly higher than that of the soft-rolled alloy. This

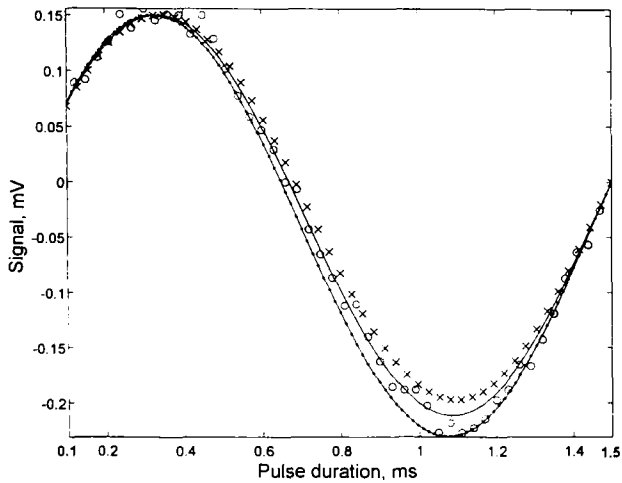


**Fig. 8.** The LIA RW pulse duration scan (in-phase) of AA100-0 Al alloy in the transmission mode: $L = 100\ \mu m$; $T_0 = 1.5$ ms; $h = 1 \times 10^5$ $W \cdot m^{-2} \cdot K^{-1}$. Circles, data; solid line, $\alpha = 1.8 \times 10^{-5}$ $m^2 \cdot s^{-1}$; crosses, $\alpha = 2.0 \times 10^{-5}$ $m^2 \cdot s^{-1}$; dotted line, $\alpha = 1.6 \times 10^{-5}$ $m^2 \cdot s^{-1}$.

**Table III.** Values of the Thermal Diffusivity of Group 2 Aluminum Foils Obtained from the Rate-Window $p_\mu$ Scan in the PTR Transmission Mode; $h = 1 \times 10^5$ W · m$^{-2}$ · K$^{-1}$

| Alloy | Thickness (mm) | Thermal diffusivity ($10^{-5}$ m$^2$ · s$^{-1}$) |
|---|---|---|
| AA1145-H18 (hard rolled) | 0.14 | $4.5 \pm 0.2$ |
| | 0.12 | $4.0 \pm 0.2$ |
| AA1100-0 (soft rolled) | 0.1 | $1.8 \pm 0.2$ |
| | 0.11 | $2.0 \pm 0.2$ |

difference in thermal diffusivities for samples within the same type of alloy may be explained only in terms of the surface roughness statistically contributing (weighing) much more in thin samples than in thick ones and changing the effective diffusivity. It is plausible that the bulk material in these samples may be a smaller thermal resistance than the equivalent resistance of the sum of two surfaces. Therefore, the thermal diffusivity values of Table III may not be considered reliable *per se* but can be very useful for qualitative evaluation/quality control of aluminum foils, especially since conventional photothermal frequency scans exhibit SNRs which are too low for any quality control assessment at all.

For the single-crystal Al plate (Group 3) the computation of the thermal diffusivity was done by fitting theoretical curves to the entire $\tau_p$ scan

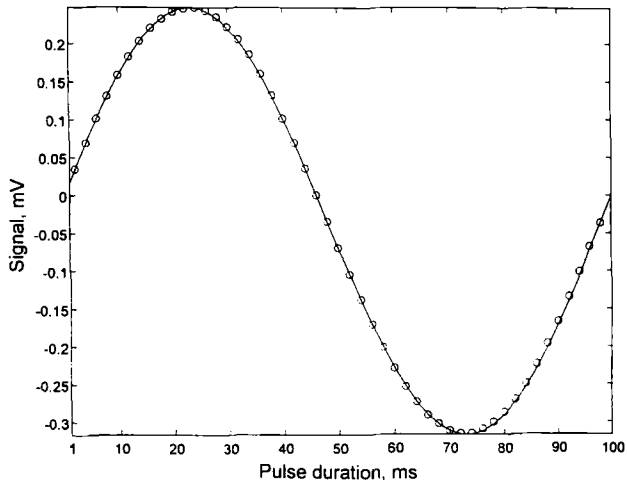


**Fig. 9.** The LIA RW pulse duration scan (in-phase) of single-crystal Al (Region 4) in the transmission mode; $T_0 = 100$ ms; $L = 2.51$ mm; $h = 1 \times 10^5$ W · m$^{-2}$ · K$^{-1}$. Circles, data; solid line, $\alpha = 9.5 \times 10^{-5}$ m$^2$ · s$^{-1}$.

experimental data in the transmission mode and obtaining excellent fits (Fig. 9). Table I gives the values of the thermal diffusivity of single-crystal Al corresponding to the various crystallographic orientations of the grains. It can be seen that the $\tau_p$-scanned RW PTR method is capable of distinguishing between widely different orientations of single-crystalline Al, yet it cannot resolve small orientational differences along the bottom of the unit stereographic-projection triangle (Fig. 2). Variations in grain surface reflectivity and uncertainty introduced by surface roughness and minute thickness variations are the most likely limiters in this measurement.

The RW measurements were. further compared with conventional and widely used PTR frequency scans [1, 17]. In these scans, it is customary to extract thermal diffusivities from the amplitude which decays with increasing frequency or from the frequency dependence of the phase shift [24]. The appropriate scanning frequency range is determined by the critical frequency of the transition between thermally thick and thin solid [25], $\mu(f) \sim L$, because then the signal is most sensitive to thermal diffusivity [18]. In terms of the model of Section 4.2, this condition is met when $|\sigma| L \sim 1$, Eqs. (36a) and (36b).

A frequency range of 4 to 43.69 Hz has been used to scan the 2-mm-thick AA6061-T6 aluminum sample (Group 1) with a 10-mm laser-beam spot size. This range has been chosen by taking into consideration the critical frequency corresponding to the thermally thick/thin boundary. It should be noted, however, that, according to Fig. 4, the $f < 20$ Hz range does not coincide with a purely 1-D theoretical interpretation of the data. Figures 10 and 11 show the amplitude and the phase of the photothermal signal, respectively, as well as the 1-D theoretical predictions from Eq. (36b). It is seen that for aluminum samples the signal amplitude conforms very well to the 1-D model for $f \geqslant 8$ Hz, but the phase of the signal does not behave as theoretically predicted. This causes problems in extracting thermal diffusivity from this channel. Therefore, the amplitude channel was chosen for the approximate determination of the thermal diffusivity of aluminum. An advantage of the frequency scan is that it is less sensitive to the $h$ coefficient than the $\tau_p$-scanned RW method. Nevertheless, to be consistent, the $h$ parameter for the frequency-domain PTR simulations has been kept the same as in the time-domain measurements. The value of thermal diffusivity obtained from the amplitude frequency scan was $(8.0 \pm 0.5) \times 10^{-5}\,\mathrm{m}^2 \cdot \mathrm{s}^{-1}$, which is consistent with the value found from the rate window method, (Table II) but with a much higher standard deviation. The rest of the samples of Group 1 were treated similarly to the 2-mm-thick sample. The results are shown in Table IV, which compares values of thermal diffusivity obtained using the frequency-domain and the rate-window PTR. Since the SNR of coadded transients was much worse

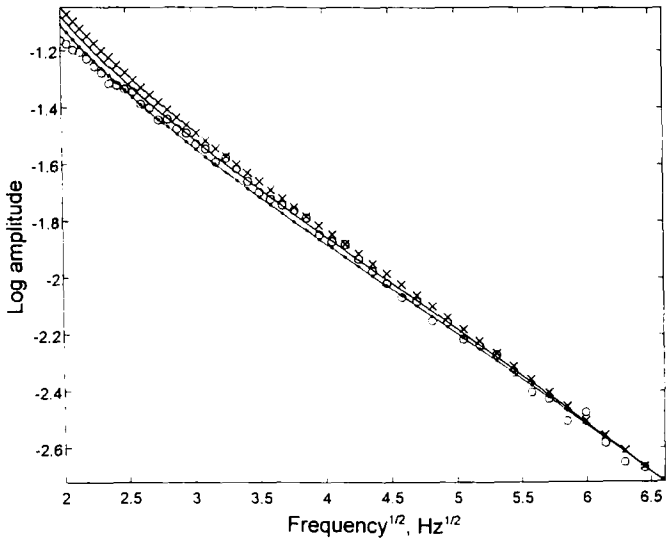


**Fig. 10.** The conventional frequency-scan amplitude of AA6061-T6 Al alloy in the transmission mode; $L = 2$ mm; $h = 1 \times 10^5$ W · m$^{-2}$ · K$^{-1}$, Circles, data; crosses, $\alpha = 7.5 \times 10^{-5}$ m$^2$ · s$^{-1}$; dotted line, $\alpha = 8.5 \times 10^{-5}$ m$^2$ · s$^{-1}$; solid line, $\alpha = 8 \times 10^{-5}$ m$^2$ · s$^{-1}$.

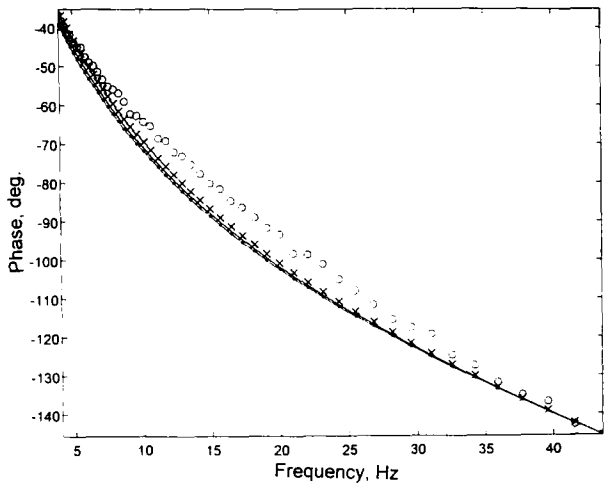


**Fig. 11.** The conventional frequency-scan phase of AA6061-T6 Al alloy in the transmission mode; $L = 2$ mm; $h = 1 \times 10^5$ W · m$^{-2}$ · K$^{-1}$, Circles, data; crosses, $\alpha = 7.5 \times 10^{-5}$ m$^2$ · s$^{-1}$; dotted line, $\alpha = 8.5 \times 10^{-5}$ m$^2$ · s$^{-1}$; solid line, $\alpha = 8 \times 10^{-5}$ m$^2$ · s$^{-1}$.

**Table IV.** Values of the Thermal Diffusivity of Group 1 AA6061-T6 Al Alloy Obtained from the Lock-In Rate-Window Pulse Duration and the Frequency Scan

| Thickness (mm) | $\tau_p$-scan method ($10^{-5}$ $m^2 \cdot s^{-1}$) | Frequence-scan method ($10^{-5}$ $m^2 \cdot s^{-1}$) |
|---|---|---|
| 2 | $7.5 \pm 0.2$ | $8.0 \pm 0.5$ |
| 1.2 | $7.5 \pm 0.2$ | $8.0 \pm 0.5$ |
| 0.5 | $7.5 \pm 0.2$ | $8.0 \pm 0.5$ |

than either of these two methods which involve narrow-band signal filtering, values of thermal diffusivity obtained with the transient response suffered from a very high uncertainty and are not presented here. Values of the thermal diffusivity of aluminum foils presented in Table III cannot be compared with their frequency-scanned counterparts, since no reliable numerical values could be obtained from curves such as in Fig. 12.

Figure 12 presents the conventional frequency-domain PTR of the Group 2 aluminum foils. These measurements have been done in the back-scattered mode using the 100- to 5102-Hz frequency range, and the amplitude channel was utilized in calculations. The $h$ parameter was the same as in the rate-window technique. Since the signal-to-noise ratio

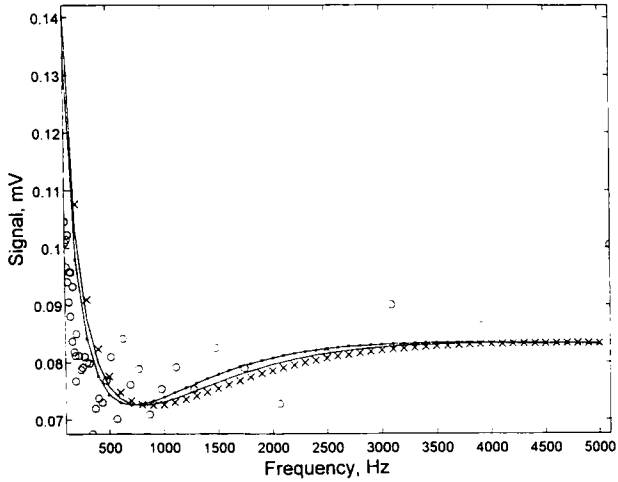


**Fig. 12.** The conventional frequency-scan amplitude of AA1100-0 Al soft-rolled foil in the backscattered mode: $L = 100$ $\mu$m; $h = 1 \times 10^5$ $W \cdot m^{-2} \cdot K^{-1}$. Circles, data; solid line, $\alpha = 1.8 \times 10^{-5}$ $m^2 \cdot s^{-1}$; crosses, $\alpha = 2.0 \times 10^{-5}$ $m^2 \cdot s^{-1}$; dotted line, $\alpha = 1.6 \times 10^{-5}$ $m^2 \cdot s^{-1}$.

(SNR) was extremely poor, especially for the soft-rolled alloy measurements, and in the absence of meaningful extrema in amplitude data, no reliable diffusivity values could be obtained. The theoretical fits shown in Fig. 12 used the best-fit values from the RW pulse-duration method (Fig. 8.).

Regarding the Group 3 single-crystal Al samples, the transmission PTR amplitude fit to the data yielded a thermal diffusivity value of $(9.5 \pm 0.5) \times 10^{-5}\ m^2 \cdot s^{-1}$ for all five regions. In comparing this value with those in Table I, it is seen that the frequency-scan method derived diffusivities, albeit in general agreement with those of the $\tau_p$-scanned RW method, are insensitive to crystallographic orientation, due primarily to the large data scatter (lower SNR) associated with frequency-domain PTR [7, 18].

## 6. DISCUSSION AND CONCLUSIONS

In 1-D frequency-domain PTR it is important to include the critical frequency of transition between thermally thick and thin regimes [25], so as to obtain the highest experimental sensitivity to the value of the bulk thermal diffusivity of a solid. For the time-domain PTR with pulse repetition period $T_0$, the thermally thick/thin transition is not so obvious. It is, therefore, necessary to check the signal phase at the 50% duty cycle point to determine compliance with the thermal thickness condition, using as the criterion the deviation from the semi-infinite reference sample signal phase ($-45°$) [3, 25]. Frequency-domain PTR is experimentally and analytically a simpler technique than the LIA RW method. To this fact alone it owes its widespread popularity. However, for high-frequency measurements the SNR and sensitivity to the absolute value of thermal diffusivity are very poor, due to the considerable decrease in the photothermal signal amplitude. This is especially true for the measurements of thin-layer axial diffusivities [18]. For instance, the uncertainty limit for soft rolled aluminum foils with frequency-domain measurements is more than $\pm 100\%$ (Fig. 12). This makes the frequency-scan method unsuitable for thermal diffusivity measurements of thin metallic samples. Furthermore, coadded transient data showed clear difficulties in measuring thermal diffusivity of good thermal conductors such as aluminum. The poor quality of data and the surface roughness contribution to the $h$ value in the backscattered mode render the transient technique inadequate for thermal diffusivity measurements of thin layers of aluminum.

For all PTR measurements, the transmission mode has been found to be less sensitive to the surface condition than the reflection mode and is therefore preferable for diffusivity measurements. The effective heat-transfer

coefficient $h$ depends on surface roughness and remains constant in the transmission mode for all samples and for all techniques employed in this work. These include the frequency range between 6.66 and 500 Hz or 2 and 150 ms in the time domain. The low $h$ values ($\sim 1000 \mathrm{W \cdot m^{-2} \cdot K^{-1}}$) obtained for the poor thermal conductors (steel and Zr–Nb alloy) are consistent with the adiabatic boundary conditions ($h \to 0$) at the metal gas interface reported by other authors [4]. The much higher values obtained for aluminum are indicators of a strong interfacial heat transfer mechanism most likely due to enhanced effusivity across the increased surface area resulting from microscopic roughness. Nevertheless, they are at variance with the temperature and heat flux continuity conditions assumed by many authors [9, 22]. The latter conditions are strictly valid in the isothermal limit $h \to \infty$.

Figures 7–9 show that it is possible to obtain excellent fits of the entire curve for the RW pulse duration scan. The uncertainty limit is $\pm 2\%$ or less for the thick samples and less than $\pm 10\%$ for Al foils. Some discrepancies between the theory and the data at longer pulse durations, especially for thin samples, may be accounted for by surface roughness and bulk inhomogeneity. Figure 13 shows the position of the RW extremum versus thermal diffusivity, using Eq. (31) coupled to the RW algorithm [18]. This figure can be used as a universal (conveniently linear) calibration curve for

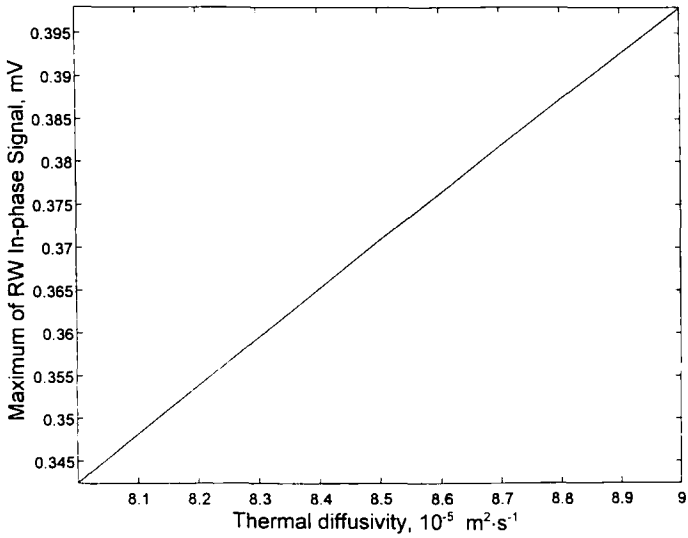


**Fig. 13.** The position of the in-phase RW extremum vs thermal diffusivity using PTR transmission with $L = 2$ mm; $h = 1 \times 10^5 \mathrm{W \cdot m^{-2} \cdot K^{-1}}$ in Eq. (31) with $x = L$.

**Table V.** Comparison of Values of the Thermal Diffusivity of Group 3 Single-Crystal Al Obtained from Lock-In Rate-Window Techniques and the Frequency Scan

| Region No. | Thickness (mm) | $T_0$-scan method ($10^{-5}\,m^2 \cdot s^{-1}$) | $\tau_p$-scan method ($10^{-5}\,m^2 \cdot s^{-1}$) | Frequency-scan method ($10^{-5}\,m^2 \cdot s^{-1}$) |
|---|---|---|---|---|
| 1 | 2.5 | $9.0 \pm 0.5$ | $8.3 \pm 0.1$ | $9.5 \pm 0.5$ |
| 2 | 2.53 | $9.0 \pm 0.5$ | $9.4 \pm 0.1$ | $9.5 \pm 0.5$ |
| 3 | 2.51 | $9.0 \pm 0.5$ | $9.5 \pm 0.1$ | $9.5 \pm 0.5$ |
| 4 | 2.51 | $9.0 \pm 0.5$ | $9.5 \pm 0.1$ | $9.5 \pm 0.5$ |
| 5 | 2.55 | $9.0 \pm 0.5$ | $9.5 \pm 0.1$ | $9.5 \pm 0.5$ |

the measurement of thermal diffusivity with good thermal conductors (aluminum, copper, brass). A similar calibration curve can be easily obtained with $h < 10^3\,W \cdot m^{-2} \cdot K^{-1}$ for poor and intermediate thermal conductors (steels, zirconium).

The RW $T_0$ scan and the frequency scan have the same uncertainty limits, with the former exhibiting a slightly improved SNR [7]. Nevertheless, it can be seen from Table V that both these techniques are relatively insensitive to orientational variations of the value of thermal diffusivity in single crystals of Al. Although the same range of values of $\alpha$ from the frequency scan and from the RW scans were obtained, the $\tau_p$-scan method is the only one which exhibits any sensitivity to crystallographic orientation. The trends shown for minimum diffusivity along a crystallographic direction close to $\langle 111 \rangle$ (Fig. 2a) are consistent with the maximum close-packed distribution of Al atoms in the $\{111\}$ planes. This implies a greater impediment to heat propagation due to the increased atomic density which increases the value of $\rho$ in the denominator of Eq. (1). A progressive increase in $\alpha$ with directional heat propagation toward the $\langle 100 \rangle$ axes is expected and indeed crudely observed in the $\tau_p$ scan of Table V. Unfortunately, the relative absence of surface quality and roughness control, coupled with the lack of Al crystals with orientations intermediate between Region 1 and all the rest (Fig. 2b), prevented any assessment of the resolution of the promising $\tau_p$-scanned PTR method to monitor the thermal diffusivity tensor in Al.

## ACKNOWLEDGMENTS

Some of the authors (E.McC., A.M., M.M.) wish to acknowledge gratefully a contract from the Manufacturing Research Corporation of Ontario (MRCO), which made this work possible. The contributions of specialty aluminum samples from ALCAN, Kingston, Ontario, are thankfully acknowledged.

## REFERENCES


1. M. Munidasa, T.-C Ma, A. Mandelis, S. K. Brown, and L. Mannik, *Mat. Sci. Eng.* **A159**:111 (1992).
2. E. V. Kudryivtsev, *Unsteady State Heat Transfer* (Iliffe Book, London,1966), p. 94.
3. H. S. Carslaw and J. C. Jaeger, *Conduction of Heat in Solids*, 2nd ed., (Oxford University, Oxford, 1959).
4. W. P. Leung and A. C. Tam, *J. Appl. Phys.* **56**:153 (1984).
5. Z.-H. Chen and A. Mandelis, *Phys. Rev. B* **46**:13526 (1992).
6. A. Mandelis and Z.-H. Chen, *Rev. Sci. Instrum.* **63**:2977 (1992).
7. A. Mandelis, *Rev. Sci. Instrum.* **65**:3309 (1994).
8. P. E. Nordal and S. O. Kanstad, *Phys. Scripta* **20**:659 (1979).
9. R. E. Imhof, B. Zhang, and D. J. S. Birch, in *Progress in Photothermal and Photoacoustic Science and Technology, Vol. II*, A. Mandelis, ed., (Prentice Hall, Englewood Cliffs, NJ, 1994), Chap. 7.
10. Supplied by ALCAN, Kingston, ON.
11. F. Kreith, *Principles of Heat Transfer* (IEP-A Dun-Donnelley, New York, 1976).
12. E. R. G. Eckert and R. M. Drake, *Analysis of Heat and Mass Transfer* (McGraw Hill, New York, 1972).
13. D. J. Crowther and J. Padet, *Int. J. Heat Mass Transfer* **34**:3075 (1991).
14. A. Mandelis, *J. Appl. Phys.* **78**:647 (1995).
15. P. M. Morse and H. Feshbach, *Methods of Theoretical Physics* (McGraw Hill, New York, 1953) p. 864.
16. W. H. Press, S. A. Teukolsky, W. T. Vetterling, and B. P. Flannery, *Numerical Methods in C*, 2nd ed. (Cambridge University Press, Cambridge, 1992), pp. 354, 366.
17. L. Qian and P. Li, *Appl. Opt.* **29**:4241 (1990).
18. M. Munidasa and A. Mandelis, Rev. Sci. Instrum. **65**:2344 (1994).
19. R. S. Quimby and W. M. Yen, *Appl. Phys. Lett.* **35**:43 (1979).
20. W. D. Lawson and J. W. Sabey, in *Research Techniques in NDT*, R. S. Sharpe, ed. (Academic, London, 1970), Chap. 4.
21. M. G. Dreyfus, *Appl. Opt.* **2**:1113 (1963).
22. D. L. Balageas, J. C. Krapez, and P. Cielo, *J. Appl. Phys.* **59**:348 (1986).
23. Y. S. Touloukian, R. W. Powell, C. Y. Ho, and M. C. Nicolaou, *Thermophysical Properties of Matter, Vol. 10* (IFI Plenum, New York, 1973).
24. X. Zhang and C. Grigoropoulos, *Rev. Sci. Instrum.* **66**:1115 (1995).
25. A. Rosencwaig and A. Gersho, *J. Appl. Phys.* **47**:64 (1976).